



The Global/Regional Integrated Model System (GRIMs): an Update and Seasonal Evaluation

Myung-Seo Koo¹ · Kanghyun Song² · Jung-Eun Esther Kim³ · Seok-Woo Son⁴ · Eun-Chul Chang⁵ · Jee-Hoon Jeong⁶ · Hyungjun Kim⁷ · Byung-Kwon Moon⁸ · Rokjin J. Park⁴ · Sang-Wook Yeh⁹ · Changhyun Yoo¹⁰ · Song-You Hong¹¹

Received: 9 June 2022 / Revised: 28 September 2022 / Accepted: 30 September 2022 / Published online: 10 October 2022
© The Author(s) under exclusive licence to Korean Meteorological Society and Springer Nature B.V. 2022

Abstract

The Global/Regional Integrated Model system (GRIMs) is upgraded to version 4.0, with the advancement of the moisture advection scheme and physics package, focusing on the global model program (GMP) for seasonal simulation and climate studies. Compared to the original version 3.1, which was frozen in 2013, the new version shows no Gibbs phenomenon in the moisture and tracer fields by implementing the semi-Lagrangian advection scheme with a better computational efficiency at higher resolution. The performance of the seasonal ensemble simulation (June–August 2017 and December 2016–February 2017) is significantly improved by new physics and ancillary data. The advancement is largest in the stratosphere, where the cold bias is dramatically reduced and the wind bias of the polar jets is alleviated, especially for the winter hemisphere. Noticeable improvements are also found in tropospheric zonal mean circulation, eddy transport, precipitation, and surface air temperature. This allows GRIMs version 4.0 to be used not only for long-term climate simulations, but also for subseasonal-to-seasonal climate prediction.

Keywords GRIMs · numerical weather prediction · general circulation model · seasonal simulation

1 Introduction

The Global/Regional Integrated Model system (GRIMs) has been developed for numerical weather prediction on operational mode as well as seasonal and climate simulations on research mode (Hong et al. 2013). This includes

global model program (GMP) for general circulation model, regional model program (RMP) for dynamical downscaling, and single-column model program (SMP) for physics development and mechanism study, thereby an integrated atmospheric model covering from global to regional scales. Since 2012, GRIMs-GMP version 3.1 has become an operational global model of the Republic of Korea Air Force (ROKAF) which is running on the ROKAF's supercomputer as well

Responsible Editor: Daehyun Kim.

✉ Seok-Woo Son
seokwooson@snu.ac.kr

- ¹ Numerical Modeling Group, Korea Institute of Atmospheric Prediction Systems, Seoul, South Korea
- ² Irreversible Climate Change Research Center, Yonsei University, Seoul, South Korea
- ³ Center for Climate/Environment Change Prediction Research, Ewha Womans University, Seoul, South Korea
- ⁴ School of Earth and Environmental Sciences, Seoul National University, 1 Gwanak-ro, Gwanak-gu, 08826 Seoul, South Korea
- ⁵ Department of Atmospheric Sciences, Kongju National University, Kongju, South Korea

- ⁶ Department of Oceanography, Chonnam National University, Gwangju, South Korea
- ⁷ Department of Civil and Environmental Engineering, Korea Advanced Institute of Science and Technology, Daejeon, South Korea
- ⁸ Division of Science Education, Institute of Fusion Science, Jeonbuk National University, Jeonju, South Korea
- ⁹ Department of Marine Sciences and Convergent Technology, Hanyang University, ERICA, Ansan, South Korea
- ¹⁰ Department of Climate and Energy Systems Engineering, Ewha Womans University, Seoul, South Korea
- ¹¹ NOAA/ESRL and CSU/CERES, Boulder, CO, USA

as the Korea Institute of Science and Technology Information's supercomputer at an approximately 25 km horizontal resolution. On research mode, it has been utilized to develop physical parameterizations for the Korean Integrated Model (KIM) at the Korea Institute of Atmospheric Prediction Systems (KIAPS), as a reference model (Hong et al. 2018). It has been also used to develop a Chemistry Climate Model (CCM) in which chemical transport model is coupled with GRIMs (Jeong et al. 2019; Lee et al. 2022).

GRIMs-GMP uses the spectral transform method as the basis for the dynamical core. This method has been widely used in global atmospheric models because of its significant computational advantages over the finite-difference method, such as its high numerical accuracy and ease of Laplacian operation (Orszag 1970; Williamson, 2007). However, the spectral approach has a fatal flaw in that negative values arise in the representation of positively defined variables because of the finite truncation in the wave space, which is known as the Gibbs phenomenon. For hydrometeors (e.g., water vapor, cloud water, and other microphysics quantities) and chemical constituents (e.g., ozone and sulfate), negative values clearly have no physical significance and should be avoided in any physical parameterization scheme for computational stability. In addition to the undershoot problem, the overshoot problem is equally serious. Unlike negative mixing ratios, overshooting is not obvious from the moisture field itself; thus, it cannot be corrected or even monitored before physical parameterizations are invoked. The overshoot can erroneously interact with parameterizations to overestimate precipitation where it occurs or to produce spurious precipitation and clouds where they do not exist.

The Gibbs phenomenon can be effectively eliminated by implementing the semi-Lagrangian advection scheme (Chang and Yoshimura 2015; Williamson 1990). Its usefulness has been tested in GRIMs-GMP. For instance, GRIMs-GMP with semi-Lagrangian moisture advection was utilized to develop cloud schemes (Han et al. 2016; Park et al. 2016) and coupling chemistry models (Jeong et al. 2019; Lee et al. 2022). However, details of its development and evaluation are not provided in the literature.

GRIMs-GMP version 3.1 has a comprehensive physics package. However, it has not been updated since 2013, although physics schemes and ancillary datasets have continuously advanced. In state-of-the-art atmospheric model such as KIM (Hong et al. 2018), for example, microphysics schemes are evolving with the consideration of mixed phase clouds and the number concentration of hydrometeor species. Scale awareness is also being adopted in boundary layer, convection, and gravity wave schemes for their gray-zone resolution. Jeong et al. (2019) tried to adopt advanced physics schemes in radiation and microphysics to couple GRIMs-GMP with chemical components, but this model was not released and confined to their own work.

Although the KIM physics package was developed based on the GRIMs framework, it is not available for the public version of GRIMs.

The purpose of this study is to update the public version of GRIMs-GMP based on Hong et al. (2013), to overcome the caveat of the old version in dynamics, and to reflect advanced physics schemes. For moisture advection, the Eulerian-based spectral scheme is replaced with a semi-Lagrangian scheme to remove the Gibbs phenomenon. The advanced physics scheme of the Weather Research and Forecast (WRF) model version 4.0 (hereafter WRF4) is adopted to update the physics schemes (https://www2.mmm.ucar.edu/wrf/users/docs/user_guide_v4/contents.html). The ancillary dataset is also updated to the recent version of datasets in better quality at a finer grid spacing, focusing on the variables with potential impacts on model performance, such as land conditions and chemical species. GRIMs-GMP version 3.1 (hereafter V3.1) uses a low-quality land condition dataset. For instance, land use and soil texture have a 100 km horizontal resolution, and the maximum snow albedo is set to a constant value. Climatological values of chemical species were also obtained from past datasets. In the new version (hereafter V4.0), these ancillary datasets are replaced with high-quality datasets with fine resolution and multidimensional variables.

The remainder of this study is organized as follows. The key information of the model update in dynamics, physics, and ancillary data is described in Section 2. The impacts of semi-Lagrangian advection scheme are quantified in Section 3 by conducting a series of idealized model experiments. Section 4 evaluates the model improvements from V3.1 to V4.0 by conducting seasonal ensemble simulations for selected winters and summers. This is followed by a discussion of the computational efficiency in Section 5. Finally, concluding remarks are presented in Section 6.

2 Model Update

The model update is presented in Table 1. Below, the updated moisture advection, physics schemes, and ancillary datasets are described in detail.

2.1 Dynamics: Semi-Lagrangian Moisture Advection

The traditional backward semi-Lagrangian scheme assumes arrival points at the regular model grid points. Similarly, the forward scheme assumes departure points at the model grid points. They require an initial guess and iterations to compute the trajectories, which means finding midpoint winds and transferring fluid particles from the departure points to the arrival points (Staniforth and Côté 1991). Unlike

Table 1 Model update description

	Target	V3.1	V3.1SL	V4.0
Dynamics	Moisture advection	Spectral		Semi-Lagrangian
Physics	Radiation	Chou et al. (1999) Chou and Suarez (1999) Chou and Lee (2005)		RRTMG_WRF4 (Iacono et al. 2008)
	Surface layer	Monin-Obuhkov (MO) (Long 1984, 1986)		MO + revision (Koo et al. 2018; Zeng et al. 2012)
	Land	Noah V2.7 (Ek et al. 2003; Mitchell et al. 2005)		Noah V3.4.1_WRF4
	Ocean	Charnock (1955) Briegleb et al. (1986) Kim and Hong (2010)		Charnock (1955) Taylor et al. (1996)
	Vertical diffusion	YSU (Hong 2010; Hong et al. 2006)		YSU_WRF4
	Gravity wave drag by orography	KA (Hong et al. 2008; Kim and Arakawa 1995)		KA_WRF4 (Choi and Hong 2015)
	Gravity wave drag by non-orography	Chun and Baik (1998); Jeon et al. (2010)		None
	Deep convection	SAS (Byun and Hong 2007; Park and Hong 2007)		KSAS_WRF4 (Han et al. 2020)
	Shallow convection	GRIMSCV (Hong and Jang 2018)		NSCV_WRF4
	Microphysics	WSM1 (Hong et al. 1998)		WSM3_WRF4 (Hong et al. 2004)
	Cloudiness	Diagnostic (Xu and Randall 1996)		Diagnostic_WRF4
Ancillary data	Vegetation fraction	16-km monthly climatology (5 y)_NCEP (Gutman and Ignatov 1998)		1-km monthly climatology (10 y)_WRFV4 (Lu et al. 2021)
	Maximum snow albedo	Constant (0.90 for vis/0.75 for nir)		5-km data (Barlage et al. 2005)
	Land use	100-km_NCEP (Hong et al. 2013)		1-km modified IGBP-DIS_WRF4
	Soil texture	100-km_NCEP (Hong et al. 2013)		1-km hybrid STATSGO- FAO_WRF4
	CO ₂	379 ppmv		400 ppmv
	Aerosol	Table (Hong et al. 2013)		100-km monthly climatology (10 y)_MACC
	Ozone	Prognostic (Hong et al. 2013)		80-km monthly climatology (10 y)_CAM5

WRF4 indicates that the relevant physics scheme is adopted from that in WRF model version 4.0

these traditional approaches, Juang (2007) proposed a new semi-Lagrangian scheme, with mass conservation, monotonicity, and positive definiteness, called the non-iteration dimensional-split semi-Lagrangian (NDSL) scheme. This scheme is a three-time-level centered scheme that requires no initial guess and no iteration for determining trajectories, because the wind is located at a regular model grid point at time t to find the departure at time $t-\Delta t$ and arrival points at time $t+\Delta t$. Zhang and Juang (2012) (hereafter ZJ2012) have proved that this new scheme is relatively simple to implement for two-dimensional (2D) limited-area modeling, and is competitively accurate compared with other

semi-Lagrangian schemes. More details, such as derivations and computational procedures, are fully described in ZJ2012.

To implement the NDSL scheme on the GRIMs, the 3D advection [$q^{n+1} = D_{SL}(q^{n-1})$] should be considered so that additional time splitting in the vertical components is necessary for the 2D NDSL scheme as follows:

$$q^{n+1*} = D_{SL}^H(q^{n-1}), \quad (1a)$$

$$q^{n+1} = D_{SL}^V(q^{n+1*}), \quad (1b)$$

where q is the tracer of interest, n is the time step, and H and V are the horizontal and vertical directions, respectively. Horizontal advection with the semi-Lagrangian scheme (D_{SL}^H), identical to ZJ2012, is first performed (Eq. 1a), and vertical advection with the semi-Lagrangian scheme (D_{SL}^V) is applied to the q^{n+1*} (Eq. 1b), which is the same as that of the time-splitting method proposed by Williamson (1990). For vertical advection on the hybrid sigma-pressure vertical coordinate (Koo and Hong, 2013), pressure and coordinated pressure velocity ($= \eta \partial p / \partial \eta$) are used for location and trajectory, respectively. A piecewise parabolic method (PPM) is used for interpolation and remapping, with a limiter preserving monotonicity (Colella and Woodward 1984; Colella and Sekora 2008). See Juang and Hong (2010) for the sensitivity test of the NDSL scheme for the interpolation method.

To avoid communication overhead from different parallel algorithms, the 1D-decomposed NDSL scheme is additionally decomposed in the vertical direction to match the GRIMs 2D-decomposition algorithm. The implemented NDSL scheme requires three transpositions (i.e., global communication between processors) at every time step, whereas more time is required for spectral advection in the transformation between the spectral and grid domains. Therefore, parallel scalability is not significantly reduced by implementing the NDSL scheme.

2.2 Physics: New Package Suite

The new physics package consists of radiative processes, surface layer parameterization, vertical diffusion, gravity wave drag, deep and shallow convections, and microphysics. The other physical parameterizations are not updated in the revised version. These are adopted from WRF4 (Table 1).

For a radiative process, the shortwave and longwave schemes are replaced with the rapid radiative transfer model for the general circulation model (RRTMG) scheme (Iacono et al. 2008). The hydrometeors are averaged over the radiation time step, and the monthly climatological variables, such as ozone and aerosols, are interpolated at a given time and model level, which are passed into the RRTMG scheme. The effective radii are set to 5.0, 10.0, and 25.0 μm for liquid clouds, ice, and snow, respectively, as a default. Additionally, the radiation-related source code was separated from the main physics package in V3.1, but it is integrated in V4.0, to make the physics code structure more readable.

The original surface layer parameterization was based on the Monin-Obuhkov similarity (Long 1984, 1986), which is revised in terms of the thermal roughness length (Zeng et al. 2012) with the inclusion of turbulent orographic form drag (Koo et al. 2018). The Noah land surface model (LSM) version 2.7.1 (Ek et al. 2003; Mitchell et al. 2005) is updated to the latest version 3.4.1 of the unified Noah LSM (<https://ral.ucar.edu/solutions/products/unified-noah-lsm>). Over the

oceans, the Charnock (1955) formula is used to calculate the roughness length for momentum, but the albedo parameterization is changed from Briegleb et al. (1986) to Taylor et al. (1996). The prognostic skin temperature scheme of Kim and Hong (2010) is excluded from V4.0.

The YonSei University (YSU) and Kim and Arakawa (KA) schemes continue to be used for vertical diffusion and orography-induced gravity wave drag, respectively, but minor updates are adopted from WRF4. For example, background diffusivity for momentum and heat is enhanced from 0.01 to 0.1 for better numerical stability in the YSU scheme and flow-blocking drag is included in the KA scheme (Choi and Hong 2015). However, the convection-induced gravity wave drag scheme (Chun and Baik 1998; Jeon et al. 2010) is deprecated in V4.0.

For deep convection, the simplified Arakawa Shubert (SAS) scheme (Byun and Hong 2007; Park and Hong 2007) is changed to a revised scheme developed by the KIAPS (called KSAS) (Han et al. 2020). Shallow convection is treated by the NCEP shallow convection scheme (SCV) instead of the GRIMs-SCV (Hong and Jang 2018). The microphysics scheme is updated from WRF-single moment class 1 (WSM1) (Hong et al. 1998) to class 3 (WSM3) (Hong et al. 2004). Cloudiness in V3.1 is diagnosed as a function of relative humidity and cloud water (Xu and Randall 1996). However, in V4.0, which is based on the cloudiness scheme option 3 in the WRF model following Mocko and Cotton (1995) and Sundqvist et al. (1989), its parameterization is more elaborated with the consideration of model resolution and cloud ice.

2.3 Ancillary Data

Regarding the land surface, the green vegetation fraction is calculated from the monthly climatology data. While V3.1 employed the 16 km dataset produced from a 5-y (April 1985–March 1991) normalized difference vegetation index (NDVI) climatology (Gutman and Ignatov 1998), V4.0 adopts the 1 km Moderate Resolution Imaging Spectrometer (MODIS)-based dataset from that used in WRF4 (Table 1). The constant value of maximum snow albedo (0.90 for visible; 0.75 for near-infrared) is replaced with MODIS based global 0.05° data (Barlage et al. 2005). The 100-km land use and soil texture are replaced with 1 km data from the International Geosphere-Biosphere Programme, Data and Information Systems (IGBP-DIS), and State Soil Geographic data-based Food and Agriculture Organization of the United Nations (STATSGO-FAO), respectively (Table 1).

Regarding the atmosphere, the carbon dioxide (CO_2) concentration changes from 379 to 400 ppmv. The new climatological aerosol dataset is adopted from the Monitoring Atmospheric Composition and Climate (MACC) project (<http://apps.ecmwf.int/datasets/data/macc-reanalysis/levty>

pe=sfc/). In V3.1, ozone concentration was predicted with climatological production and loss term, while it is prescribed in V4.0 by the 10-y climatological value obtained from the Copernicus Atmosphere Monitoring Service (CAMS) dataset (<https://www.ecmwf.int/en/forecasts/dataset/cams-global-atmospheric-composition-forecasts>).

3 Idealized Simulation

As 2D idealized tests of the NDSL scheme have already been conducted with respect to mass conservation and shape-preserving interpolation in ZJ2012, such tests are omitted in this study. Instead, the performance of the 3D NDSL scheme is evaluated for standard idealized test beds on a sphere based on the 2012 Dynamical Core Model Intercomparison Project (DCMIP) (Ullrich et al. 2012). The initial conditions and a simple physics package can be obtained from <https://earth.systemcog.org/projects/dcmip-2012/>. A brief description of the idealized testbeds is provided in Table 2.

According to the set of 3D tracer transport test beds as presented in Kent et al. (2014) (hereafter K2014), Fig. 1 shows the simulation results for 3D passive advection at a T126L60 resolution, where T126L60 indicates that the truncated wave number is 126 with 60 vertical layers. In accordance with K2014, a terrain-following pressure-based vertical coordinate is used with uniformly spaced vertical layers ($\Delta z = 200$ m) and a model top of 12 km (~ 254.944 hPa).

For deformational flow, the initial field of tracers q_1 , q_2 , q_3 , and q_4 represents two cosine bells centered at 150°E and 150°W on the equator, which are advected along the prescribed 3D wind fields and returned to the original location in 12 d. The field of the first tracer (q_1) has a maximum value of 1 at the center point of each cosine bell, and the values gradually decrease to the background value of 0 as they approach the boundary of each cosine bell. Similarly, the field of the second tracer (q_2) has a minimum value of 0.1 at the center point of each cosine bell, and the values gradually increase to the background value of 0.9 as they go to the boundary

of each cosine bell. The field of the third tracer (q_3) has only two values: 1 for two cosine bells and 0.1 for the background. The field of the fourth tracer (q_4) is determined as $q_4 = 1 - 0.3(q_1 + q_2 + q_3)$. Refer to K2014 for detailed specifications of the experimental design for the tracers. Figure 1a–b show the tracer q_3 at the 4,900 m height level and time $t = 6$ and 12 d. The plot at $t = 6$ d shows that the spectral advection exhibits a wavelike pattern with spurious overshoots and undershoots in regions where the background value is 0.1. This is attributed to the spectral transform (Fig. 1a). The overshoot is discernible in the deformed cores, where the initial value is 1.0. The maximum and minimum values are 1.132 and 0.005, respectively, whereas the exact values range from 0.1 to 1.0. The semi-Lagrangian advection produces almost the same result as spectral advection, except for regions of overshoots and undershoots that are not visible (Fig. 1b). Although the maximum of the semi-Lagrangian advection (0.877) at T126 ($1^\circ \times 1^\circ$) resolution is underestimated because of the interpolation, the magnitude becomes closer to 1 as model resolution increases, as it is 0.955 and 0.987 at T254 ($0.5^\circ \times 0.5^\circ$) and T510 ($0.25^\circ \times 0.25^\circ$) resolution, respectively. The background minimum value is preserved at 0.1 regardless of the resolution. The resulting tracer fields at the final time, $t = 12$ d, are comparable. Although the two cores are smoother, the values are not overestimated in the semi-Lagrangian advection. For tracers q_1 , q_2 , q_3 , and q_4 (see K2014 for further details), the normalized error norms are computed as follows:

$$l_1(q) = \frac{\sum |q - q_i|}{\sum |q_i|}, \tag{2}$$

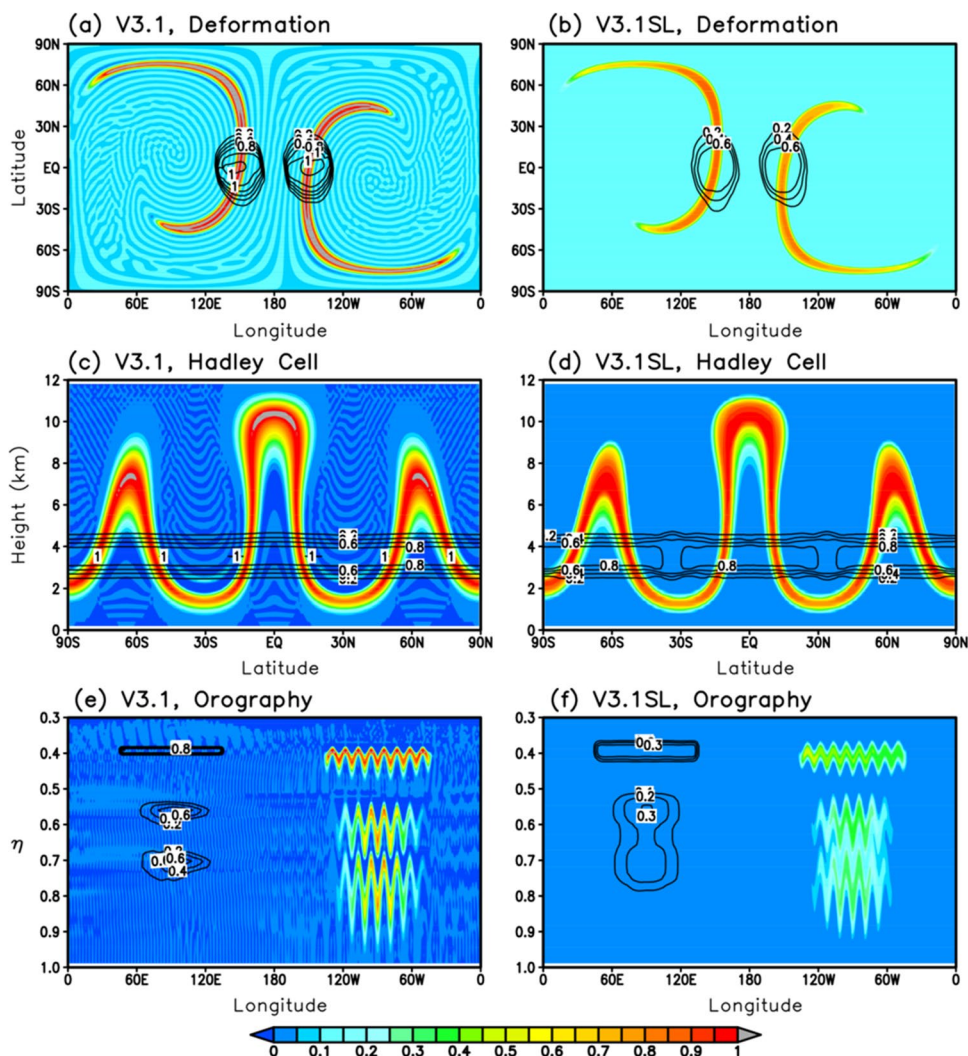
$$l_2(q) = \sqrt{\frac{\sum (q - q_i)^2}{\sum q_i^2}}, \tag{3}$$

$$l_\infty(q) = \frac{\max |q - q_i|}{\max |q_i|}, \tag{4}$$

Table 2 Summary of 3D idealized test beds

	Passive advection			Moist baroclinic wave
	Deformation	Hadley Cell	Orography	
Integration period	12 d	24 h	12 d	15 d
Horizontal Resolution	T126 ($\sim 1^\circ$) T254 ($\sim 0.5^\circ$) T510 ($\sim 0.25^\circ$)			
Vertical layers	30 60 120			30
Dynamic update	X			O
Physics forcing	X			Large-scale condensation

Fig. 1 **a–b** Deformational-flow test; latitude–longitude plot of tracer q_3 at a height of 4,900 m at day 6 (shading) and day 12 (contour). **c–d** Hadley-like meridional circulation test; latitude–height plot of tracer q_1 at longitude 180° at hour 12 (shading) and hour 24 (contour). **e–f** Orography test; longitude– η plot of tracer q_4 at latitude 0° at day 6 (shading) and day 12 (contour). The (left) spectral and (right) semi-Lagrangian advection are conducted at T126L60 resolution. The contour interval is 0.2, but 0.1 for (f)



where q_i is the tracer field at the initial time, which is also the exact solution at the final time owing to periodicity. In Table 3, the error norms are generally comparable between the spectral and semi-Lagrangian advectations at T126L60 resolution. The normalized error norms for all tracers decrease with increasing horizontal resolution from T62 to T254 for the L60 vertical layers. Increasing the vertical resolution from L60 to L120 for the T254 horizontal resolution provides a slight improvement, but not a significant change in normalized error norms. The convergence rates of normalized error norms are relatively poor for the semi-Lagrangian advection than that of the spectral advection. Although not presented, the mixing diagnostics and correlation plot demonstrates that no overshoots and undershoots occur for the semi-Lagrangian advection with monotone limiter in which more realistic mixing is produced than that of spectral advection. The error scores are comparable to those of K2014.

These features also appear in the Hadley-like meridional circulation test (Fig. 1c–d), in which the initial tracer field

consists of a single layer between 2,000 and 5,000 m that is deformed during the 24-h period. In Fig. 1c, overshoots (values higher than 1) are evident in the core region for spectral advection at hours 12 and 24. A more serious issue is that spectral advection generates negative values in regions where the tracer is out of existence. The semi-Lagrangian advection well reproduces the vertically deformed tracer field at hour 12, with no negative values (Fig. 1d). However, it yields gaps in the final tracer at approximately 30°N and 30°S, as in K2014, presumably due to the extreme stretching that takes place in this area of the tracer, which is speculated to diminish with the increase in vertical resolution.

A more remarkable difference is observed in the horizontal advection test of thin cloud-like tracers in the presence of orography (Fig. 1e–f). Three cloud-like tracers at 3,050 m, 5,050 m, and 8,200 m were horizontally advected over a Schär-like (Schär et al. 2002) mountain with a 2,000 m high peak. For spectral advection (Fig. 1e), the tracers move up and down over the mountain range (135°W–45°E), but the magnitude of fluctuation

Table 3 Normalized error norms for the tracers [q1, q2, q3, and q4] at day 12, simulated from the semi-Lagrangian advection at various resolutions and spectral advection at T126L60 resolution

Resolution		q_1	q_2	q_3	q_4
T62L60	l_1	0.4713	0.0012	0.0225	0.0012
	l_2	0.3562	0.0147	0.2620	0.0138
	L_∞	0.4351	0.3811	0.8372	0.4099
T126L60	l_1	0.2052	0.0005	0.0181	0.0009
	l_2	0.1792	0.0072	0.2335	0.0117
	L_∞	0.3833	0.3226	0.8353	0.4039
T126L60 (spectral)	l_1	0.2590	0.0006	0.0178	0.0009
	l_2	0.1613	0.0061	0.2098	0.0108
	L_∞	0.2666	0.2210	0.8929	0.4071
T254L60	l_1	0.1585	0.0004	0.0152	0.0007
	l_2	0.1511	0.0057	0.2079	0.0102
	L_∞	0.3573	0.3030	0.8300	0.3768
T254L90	l_1	0.1347	0.0003	0.0129	0.0006
	l_2	0.1366	0.0052	0.1901	0.0094
	L_∞	0.3407	0.3105	0.8759	0.3842
T254L120	l_1	0.1276	0.0003	0.0113	0.0005
	l_2	0.1351	0.0049	0.1758	0.0087
	L_∞	0.3335	0.2938	0.8754	0.4033

decreases with height because the hybrid vertical coordinate system smoothly changes from terrain-following levels near the ground to isobaric surfaces in the upper layers. The returned tracers on day 12 are comparable to their initial state, but the bottom two tracers are slightly underestimated. Although the semi-Lagrangian advection manages to enable the tracers to follow terrain, the simulated fields are considerably smooth, and the two bottom tracers become connected (Fig. 1f). This is caused by both interpolation remapping and monotonous filtering of the NDSL scheme. In addition to the increase in the model resolution, a more accurate method for interpolation and monotonicity is required to alleviate such diffusive features.

To check whether moisture interaction is working normally between the 3D dry dynamical core and the semi-Lagrangian moisture advection scheme, the moist baroclinic wave test is performed by adding a moisture equation to the dry baroclinic wave test (Lauritzen et al. 2010) and by considering the original temperature equation (dry-surface pressure) as an equation for the virtual temperature (moist-surface pressure). Only small differences are found (not shown) in the evolutions of moist and dry baroclinic waves simulated from spectral and semi-Lagrangian advection up to day 15, which can be the first sensitivity check for moisture interaction. In addition, the potential temperature dynamically advected by the NDSL scheme does not differ

much from that calculated by the simulated temperature on day 9.

Ullrich et al. (2012) stated that the inclusion of a large-scale condensation process can provide a feedback mechanism between the equations of motion and moisture because the excess moisture is removed as large-scale precipitation without a cloud stage or re-evaporation, and the released heat forces the thermodynamic variable. Along with the consideration of dry-air adjustment for mass conservation, Fig. 2 shows the result of the moist baroclinic wave test with large-scale condensation on day 9, when the grid effects are more pronounced. At T254L30 resolution following the DCMIP protocol, the spectral advection reproduces the surface pressure well with no grid imprint over the globe, whereas a noisy wave is observed at the surface (Fig. 2a). The pattern of the semi-Lagrangian-simulated surface pressure follows that of the spectral run well, without the noisy wave (Fig. 2b). The lowest surface pressures are 931.2 and 932.7 hPa for the spectral and semi-Lagrangian runs, respectively. For a relative humidity of 850 hPa, spectral advection produces wavelike relative humidity at high latitudes (Fig. 2c) as moisture is spuriously generated by spectral advection. Such noise are clearly removed in the semi-Lagrangian advection (Fig. 2d). Noise-like relative humidity of 20% is commonly discernible for both runs.

The impact of semi-Lagrangian advection on hydrometeors is further examined. Figure 3 shows the sum of all hydrometeors and total cloud cover simulated from the spectral and semi-Lagrangian runs, with full physics at T126L64 resolution. The new cloud microphysics scheme is used here, which considers moisture in three categories: water vapor, cloud liquid water and cloud ice, and rain and snow (Table 1). On forecast day 2, the spectral run yields artificial hydrometeors that are numerically generated because of spectral transformation, whereas no spurious hydrometeors are observed, but the major pattern is preserved in the semi-Lagrangian run (Fig. 3a–b). In V3.1, cloudiness is calculated by considering not only the relative humidity but also the sum of the hydrometeors. Accordingly, spurious hydrometeors lead to inaccurate total cloud cover. For the spectral run, cloudiness is globally widespread at a model layer $\eta=0.5$, where the semi-Lagrangian-simulated cloudiness is clear sky (Fig. 3c–d). This feature occurs in all model layers and influences the interaction between clouds and radiation.

4 Seasonal Ensemble Simulation

In this section, we assess the general characteristics and systematic biases of V3.1, V3.1SL, and V4.0. Seasonal integration is conducted by prescribing the observed sea surface temperature (SST). Both the initial and surface boundary conditions are obtained from the National Center

for Environment Prediction (NCEP) Global Forecast System (GFS) analysis. Major surface forcings (SST and sea ice concentration from NCEP-GFS analysis; green vegetation fraction and snow-free surface albedo from climatology data) are prescribed with daily updates. Background CO₂, aerosols, and ozone are updated at every time step with climatological values. The climatological input data are updated along with physics in V4.0 (Table 1).

Three experiments, V3.1, V3.1SL, and V4.0, are conducted by varying the model configuration (Table 1). Each experiment comprising 10 ensemble members is initialized at 00 UTC from the 1st to 10th of November 2016 and May 2017, and integrated for four months onward. The first month is discarded as a spin-up period, and the ensemble averages of ten members for the last three months are analyzed, that is, June to August (JJA) 2017 for the boreal summer and December 2016 to February 2017 (DJF 2016–2017) for the boreal winter. The horizontal resolution is set to T126 (~100 km) and the vertical resolution is 64 levels with a model top at 0.3 hPa (~55 km) on the hybrid sigma-pressure vertical coordinate.

Figure 4 shows the vertical structures of the zonal-mean zonal wind (U), meridional wind (V), temperature (T), and specific humidity (Q) for JJA 2017 in each experiment. V3.1 adequately reproduces the zonal-mean zonal wind in the troposphere in comparison to the ERA-Interim data (Fig. 4a). The subtropical jet is located around 30°S at 200 hPa in the southern hemisphere (SH) and around 45°N in the northern hemisphere (NH). Although not statistically significant, its amplitude is stronger than that of ERA-Interim by approximately 3–4 m s⁻¹ in the SH, but weaker in the NH (Fig. 4a). The stratospheric polar vortex in the SH is reproduced well by the model, but its amplitude is slightly underestimated. Unlike the extratropics, the zonal wind in the equatorial stratosphere is poorly simulated and characterized by positive and negative biases in the vertical direction. These biases result from the failure to simulate the Quasi-Biennial Oscillation (QBO), which is a common problem in climate models (Butchart et al. 2018).

There is little bias in the zonal-mean meridional wind, excluding the dipolar bias in the tropical upper troposphere (Fig. 4b). Negative and positive meridional wind biases are found on the upper and lower sides of the negative wind in the troposphere, respectively. This likely results from a higher tropopause in the model than in the reanalysis, due to cold biases in the stratosphere (Fig. 4c). A higher tropopause allows a vertically extended Hadley circulation, causing the southward wind in the equatorial upper troposphere to be located at a higher level than the observed one.

Cold biases were detected throughout the stratosphere in both hemispheres (Fig. 4c). These biases, which are colder than -5 K, start to increase at the 200 hPa pressure level in the extratropics and the 100 hPa level in the tropics. These levels correspond to the tropical tropopause

layer, where static stability changes dramatically. In the lower troposphere, considerable warm biases are observed over the Arctic, possibly owing to the overestimation of cloudiness and misrepresentation of near-surface processes, such as the fluxes associated with land surface, snow cover, and sea ice extent. Figure 4d shows that the specific humidity is underestimated in the tropical and subtropical lower troposphere, whereas it is slightly overestimated in the NH high latitudes. These biases highly correspond with those of V3.1SL for all the prognostic variables (Fig. 4e–h), and the similarity in the bias pattern between V3.1 and V3.1SL is confirmed for DJF 2016–2017 (Fig. 5a–d versus e–h).

Figure 4i–l present the zonal-mean zonal wind, meridional wind, air temperature, and specific humidity in the V4.0. The biases of zonal wind are not very different from those of V3.1 and V3.1SL, but its magnitude is slightly amplified. For instance, the negative bias of jet around 60°S above 300 hPa is extended further to the near surface, and the dipole pattern of stratospheric zonal wind biases in the tropics is strengthened (Fig. 4i). The vertical dipole pattern of meridional wind biases observed in V3.1 and V3.1SL disappears in V4.0 (Fig. 4j) possibly due to the reduced temperature biases in the stratosphere (Fig. 4k). However, a weak meridional dipole pattern is still found, leading to meridional convergence anomaly at the 200 hPa northerly wind core. The amplitude of meridional wind biases is reduced in the V4.0 compared to the V3.1SL. For DJF 2016–2017, V4.0 properly alleviates the biases of zonal wind in the stratosphere (Fig. 5i) and the dipolar bias of the meridional wind in the tropical upper troposphere (Fig. 5j). Dramatic improvement of model biases is found in the stratospheric temperature (Fig. 4k). The temperature biases in the whole stratosphere are substantially reduced in the V4.0. The cold biases in the tropical tropopause layer are also decreased to less than -1 K. The reduced biases are more prominent for DJF 2016–2017 (Fig. 5k). Figures 4 and 5 L further show that dry and wet biases still exist in V4.0, but their magnitudes are somewhat reduced.

Figure 6 displays the stationary eddy of the 500 hPa geopotential height (GPH) in V3.1SL and V4.0. The results of V3.1 are like those of V3.1SL and are not displayed hereafter to focus on the impacts of the updated physics package. Here, the stationary eddy is defined as the deviation from the zonal mean with the time mean for JJA 2017 and DJF 2016–2017. The V3.1SL captures the planetary-scale wave patterns, as in the ERA-Interim data, with a spatial correlation of 0.69 for JJA 2016 and 0.81 for DJF 2016–2017 (Fig. 6b and e). Relatively large errors are found in the winter hemisphere, but the planetary-scale wave patterns are still well simulated (compare the contours in Fig. 6b and e and those in Fig. 6a and d). For JJA 2017, V4.0 shows a better resemblance to the observed

pattern, with a higher pattern correlation of 0.80 (Fig. 6c). In DJF 2016–2017, although a dipole pattern over the Eurasian continent is smoothed, the V4.0 performance is still robust in the simulation of the 500 hPa GPH stationary eddies (Fig. 6f).

The zonal-mean poleward momentum and heat fluxes of the stationary and transient eddies are shown in Figs. 7 and 8. When compared to the ERA-Interim data, the biases are prominent at high latitudes, especially in the winter hemisphere. This is consistent with the mean biases of the model (Figs. 4 and 5). Unlike eddy heat fluxes, whose biases are limited in the stratosphere, eddy momentum fluxes show large biases in the troposphere around 65°S in JJA (Fig. 7b–c) and 60°N in DJF (Fig. 8b). Such biases indicate that the model exaggerates equatorward eddy momentum fluxes on the poleward flank of the mid-latitude jet, consistent with negative zonal wind biases on the poleward side of the eddy-driven jet (Figs. 4e and i, and 5e).

Despite the similarity in the eddy flux biases of V3.1SL and V4.0, the latter shows smaller biases. The reduced biases in V4.0 are particularly evident in the polar stratosphere. This improvement could be partly attributed to the introduction of new low-level drag parameterizations: (1) flow-blocking

drag in the orography-induced gravity wave scheme, and (2) turbulent orographic form drag in the surface layer scheme (Table 1). Koo et al. (2018) shows that polar stratospheric wind and temperature can be highly modulated by low-level drag.

The poleward eddy momentum and heat fluxes (positive in the NH) are associated with equatorward and upward group velocities of Rossby waves (Edmon et al. 1980). In this regard, these biases can be interpreted as the upward wave energy propagation and equatorward refraction in the high-latitude stratosphere being underestimated in the model, while the poleward wave energy propagation in the troposphere is exaggerated. The latter may result from weaker wave reflection at high latitudes compared to the ERA-Interim data. As shown in Figs. 4, 5, 7 and 8 that the model shows a weaker polar vortex, although the wave energy propagation in the stratosphere is weaker. Given that the stratospheric polar vortex becomes strong when wave activities are weak, this result may suggest that the stratospheric mean biases originate not only from dynamic processes but also from thermodynamic processes.

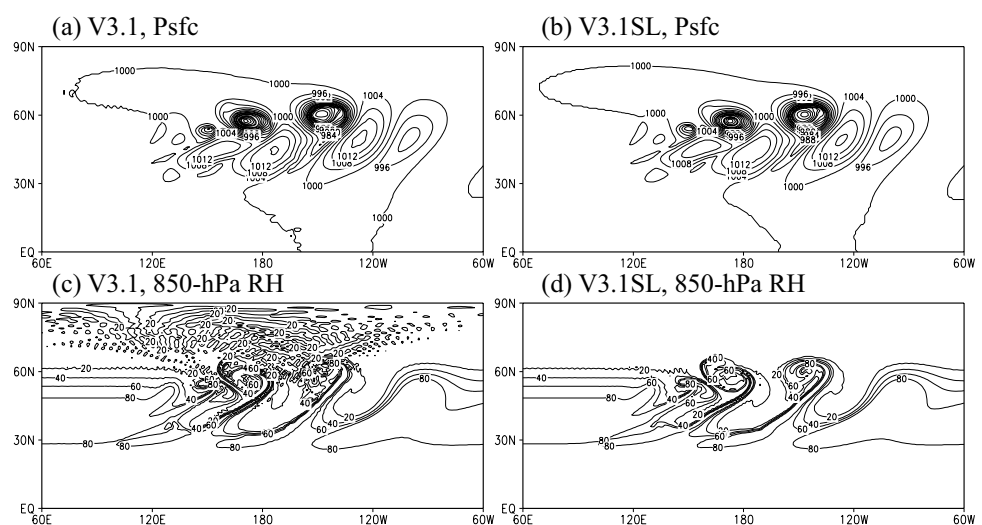
Precipitation patterns are illustrated in Fig. 9, and skill scores are tabulated in Table 4 for JJA 2017 and DJF 2016–2017. V3.1SL and V4.0 capture the main structure

Table 4 Global mean, root-mean-square error (RMSE; land/ocean), and pattern correlation coefficient (PC) for seasonally-averaged precipitation amount (mm day⁻¹) simulated by V3.1SL and V4.0, against the GPCP data for JJA 2017 and DJF 2016–2017

	JJA 2017			DJF 2016–2017		
	Global mean (GPCP=2.68)	RMSE	PC	Global mean (GPCP=2.67)	RMSE	PC
V3.1SL	3.21	2.33 (1.80/2.51)	0.754	3.12	2.29 (1.76/2.47)	0.744
V4.0	2.49	2.08 (1.69/2.21)	0.721	2.39	1.93 (1.93/1.93)	0.719

Bold indicates the better skill scores

Fig. 2 Moist baroclinic wave with large-scale condensation: **a–b** Surface pressure (Psfc; hPa) and **c–d** 850 hPa relative humidity (RH; %) at day 9, simulated from (left) V3.1 and (right) V3.1SL at T254L30 resolution. The contour intervals are 4 hPa and 20% for surface pressure and 850 hPa relative humidity, respectively



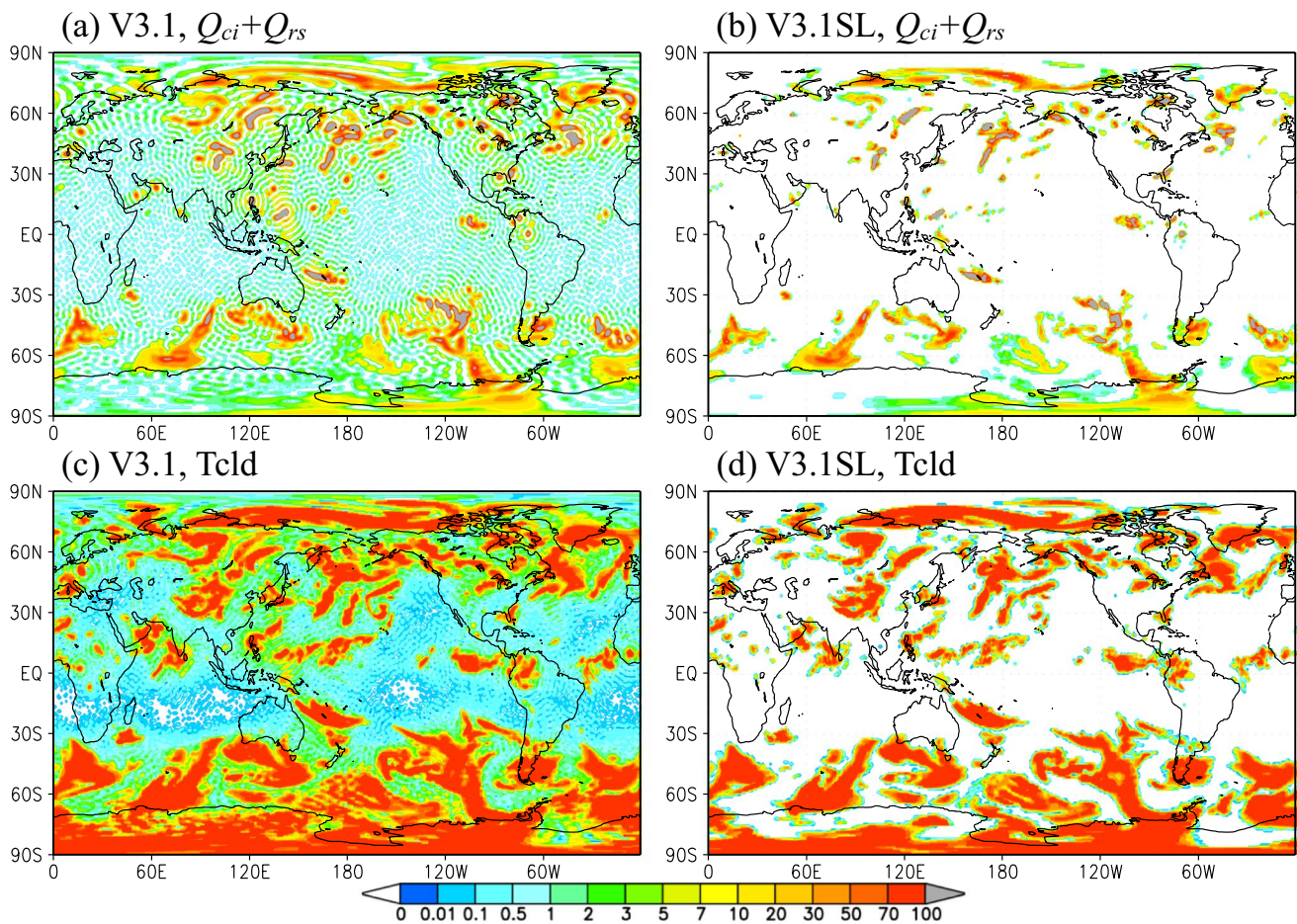


Fig. 3 a–b Sum of hydrometeors (mg kg^{-1}) and c–d total cloud cover (Tcld; %) at $\eta \approx 0.5$ at day 2, simulated from (left) V3.1 and (right) V3.1SL at T126L64 resolution. Both V3.1 and V3.1SL employ the WSM3 scheme for microphysics here, instead of WSM1 scheme

of the Global Precipitation Climatology Project (GPCP) monthly data (Adler et al. 2018) reasonably well. However, the V3.1SL tends to overestimate the global precipitation amount by approximately 15–20%, with spurious light precipitation prevailing across the globe (Fig. 9b and e). Overestimation is particularly evident in the precipitation core regions, such as the inter-tropical convergence zone, Indian Ocean warm pool, and mid-latitude of the Pacific and Atlantic Oceans. In V4.0, such spurious light precipitation and overestimated precipitation cores are alleviated (Fig. 9c and f). The global mean precipitation amount (right upper end in each plot) is underestimated by 7–11% compared to the observation, especially over land such as South Africa in JJA 2017 and South America in DJF 2016–2017. By updating the physics package in V4.0, the ratio of convective precipitation amount to total precipitation amount is increased over the ocean, while it decreases over land (Fig. S1a). The amount of precipitable water becomes larger than that in the old version (Figure S1b), and the outgoing longwave flux at

the top of the atmosphere generally reduces (Fig. S2). This may be linked to moistening in the lower troposphere of the tropics by the updated microphysics, convection, and radiation schemes in V4.0 (Table 1). For a more robust evaluation, an in-depth sensitivity study with long-term simulations should be conducted in future research.

Figure 10 shows the difference in the inland 2-m air temperature between the model simulations and ERA-Interim data. For JJA 2016, V3.1SL exhibits warm biases over Eurasian and North American continents (Fig. 10a). A large warm bias is found over Antarctica, whereas cold biases appear only in limited regions such as North Africa and Australia (Fig. 10a). These warm and cold biases are significantly reduced in V4.0 (Fig. 10b). For DJF 2016–2017, V3.1SL shows warm biases around the Arctic but cold biases over the NH continents (Fig. 10d). These biases are again reduced in V4.0 (Fig. 10e). This improvement is likely related to the update of near-surface physics, such as the radiation scheme and land surface model (Table 1). The new ancillary dataset

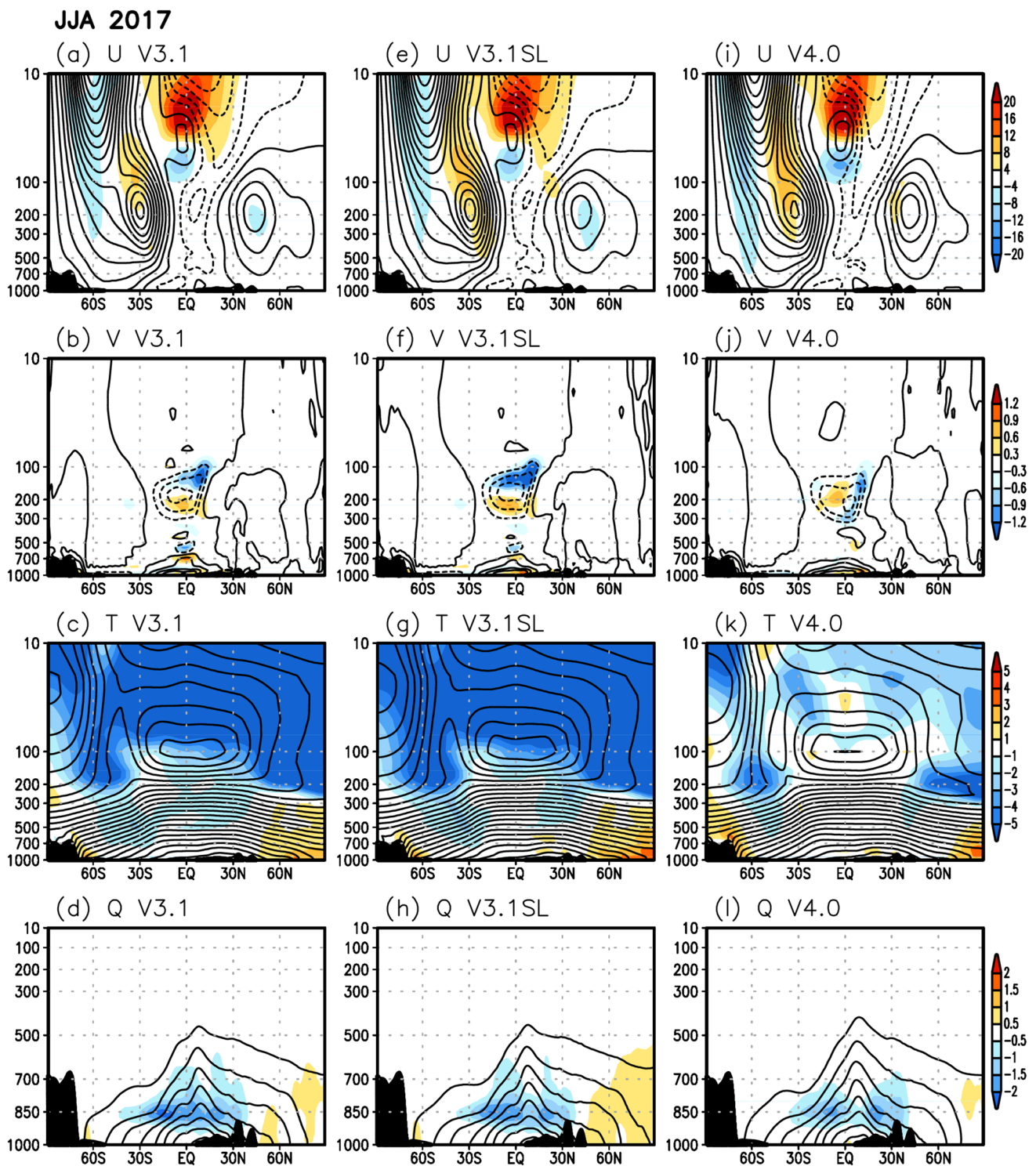


Fig. 4 Vertical cross-sections of zonal mean **a, e, i** zonal wind (contour interval: 5 m s^{-1}), **b, f, j** meridional wind (contour interval: 1 m s^{-1}), **c, g, k** temperature (contour interval: 5 K), and **d, h, l** specific humidity (contour interval: 2 g kg^{-1}) for JJA 2017, simulated by **a–d** V3.1, **e–h** V3.1SL, and **i–l** V4.0. Contour indicates the model mean

values and shading shows the difference from the ERA-Interim data. Y-axis is displayed on the logarithmic scale, except for the specific humidity. The topography is masked out by the black-shaded area for the reliable comparison

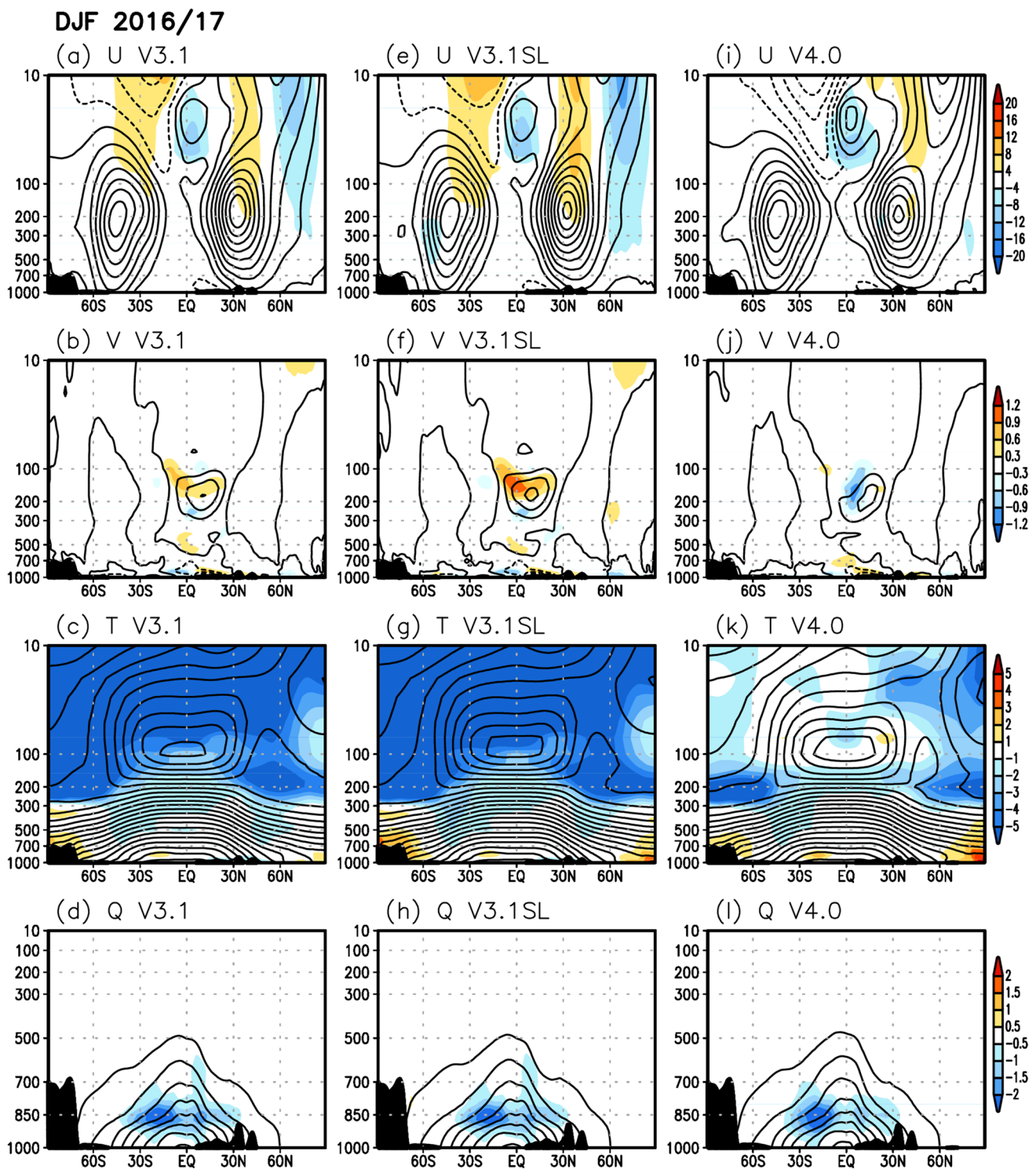


Fig. 5 Same as Fig. 4, but for DJF 2016–2017

of the maximum snow albedo is another potential source of model improvement. However, the warm biases in the winter hemisphere pole remain in V4.0. This may indicate that the interaction between the atmosphere and land surface, such as the fluxes from snow and ice, needs to be further enhanced.

5 Computational Efficiency

The computational cost of the updated model is briefly described in this section. The total computational cost, including I/O processes, increases by approximately 20%

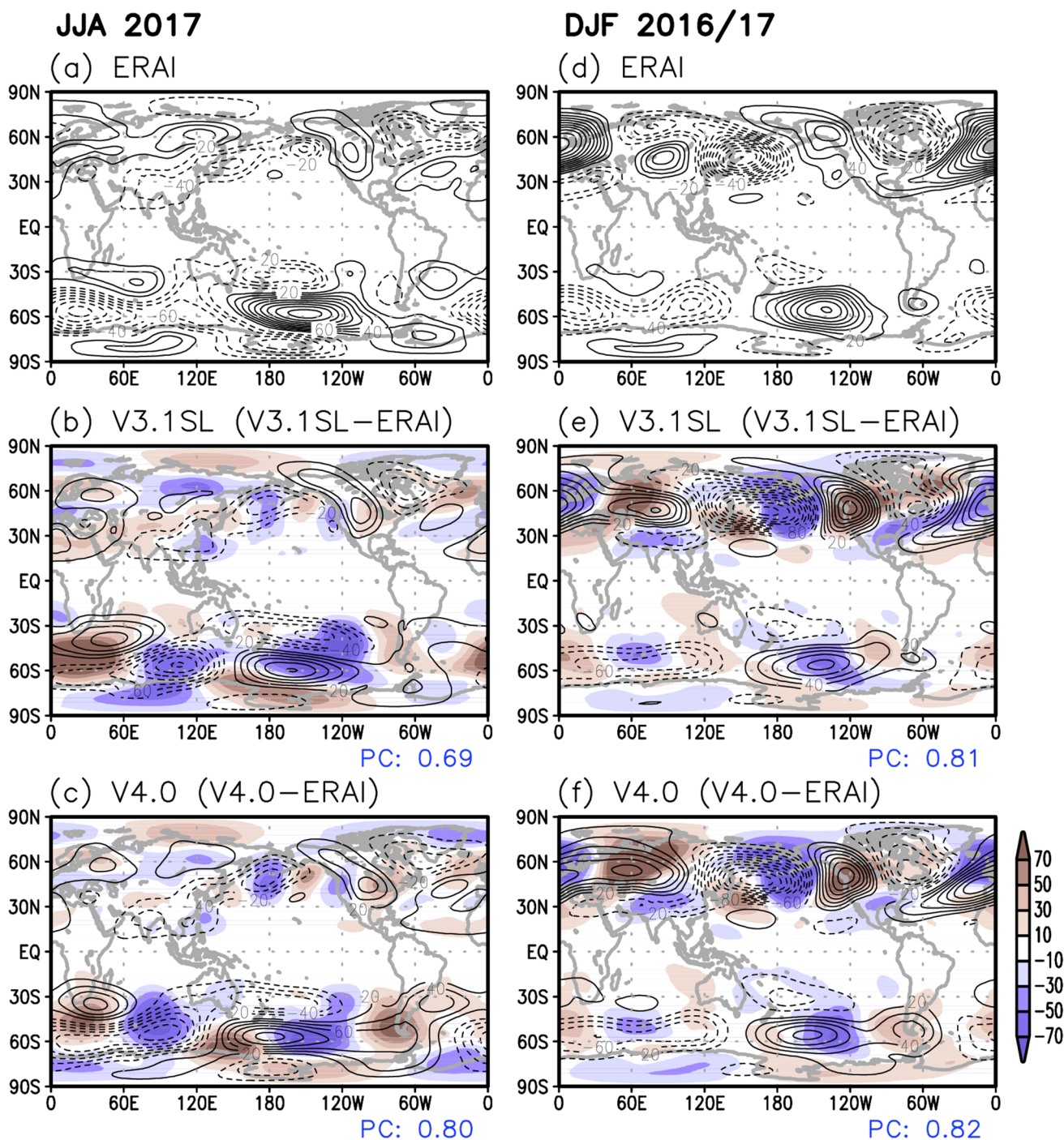


Fig. 6 Stationary eddy of the 500-hPa geopotential height (contour, interval: 20 m) for (left) JJA 2017 and (right) DJF 2016–2017, obtained from **a, d** ERA-Interim and simulated by **b, e** V3.1SL and **c, f** V4.0. Shading designates the biases from the reanalysis. The pattern correlations between the model and the reanalysis are shown at the bottom of each plot

from V3.1 to V4.0 at T126L64 resolution. This mainly results from the additional interpolation steps in semi-Lagrangian scheme and the additional hydrometeors in WSM3.

Figure 11 compares the total wall-clock times of spectral advection (W_{CTL}) and semi-Lagrangian advection (W_{SL}) with

four tracers (WSM3 + 1) at T62, T126, T254, and T510 resolutions with 64 vertical layers. The computational efficiency of the semi-Lagrangian advection is then calculated as $[1 - W_{SL}/W_{CTL}] \times 100$. When the ratio is greater than 0, the semi-Lagrangian advection is more efficient than the spectral advection. At relatively low resolutions (T62 and T126), the

four tracers (WSM3 + 1) at T62, T126, T254, and T510 resolutions with 64 vertical layers. The computational efficiency of the semi-Lagrangian advection is then calculated as $[1 - W_{SL}/W_{CTL}] \times 100$. When the ratio is greater than 0, the semi-Lagrangian advection is more efficient than the spectral advection. At relatively low resolutions (T62 and T126), the

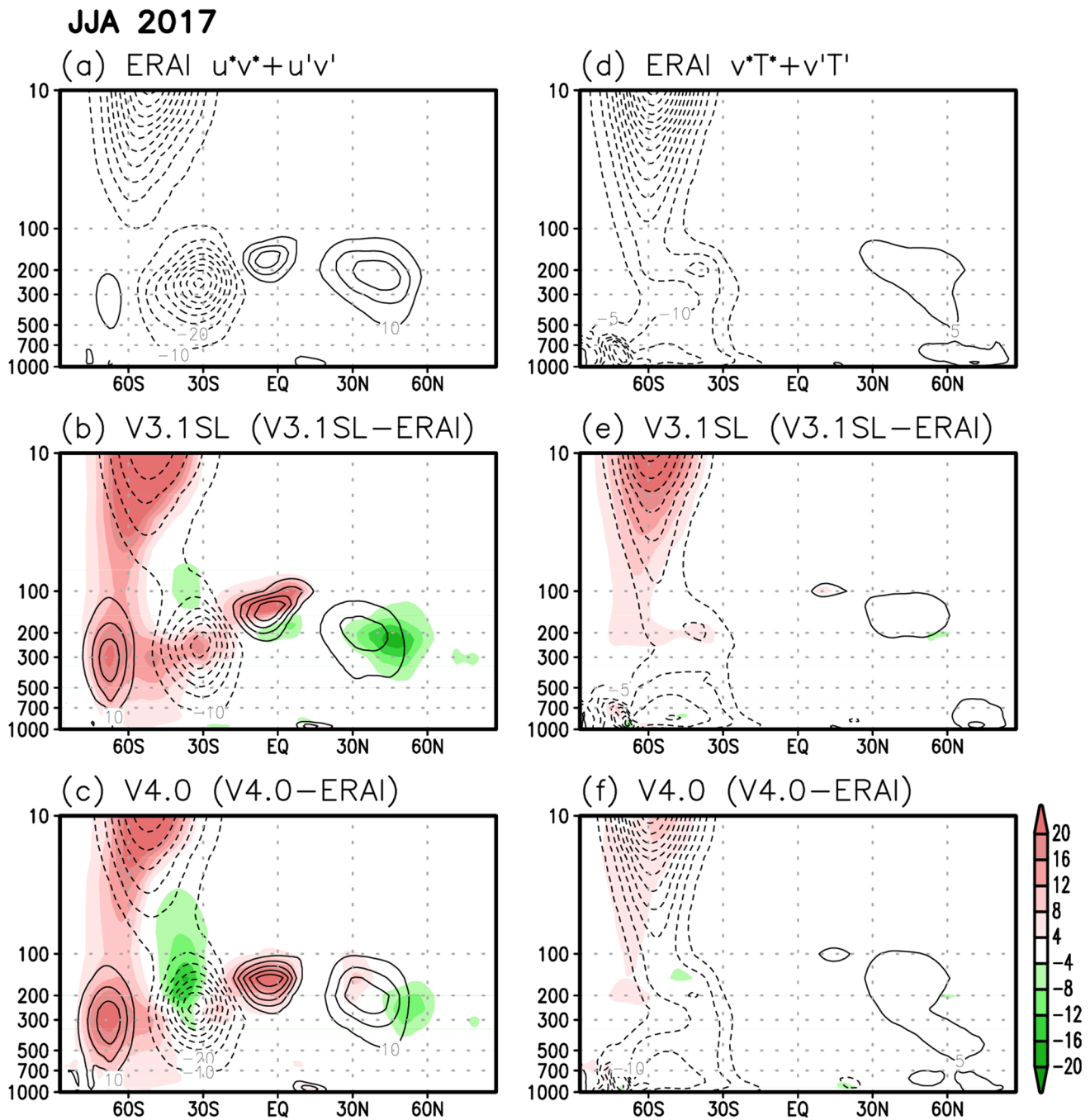


Fig. 7 Meridional cross-section of the zonally-averaged northward flux of **a–c** zonal momentum ($\text{m}^2 \text{s}^{-2}$) and **d–f** temperature (K m s^{-1}) by stationary and transient eddies for JJA 2017, obtained from

a,d ERA-Interim and simulated by **b,e** V3.1SL and **c,f** V4.0. Shading indicates the biases from the reanalysis. The contour intervals are $10 \text{ m}^2 \text{s}^{-1}$ in (a)–(c) and $5 \text{ m}^2 \text{s}^{-1}$ in (d)–(f)

semi-Lagrangian advection requires more computation cost than the spectral advection. However, the opposite trend is observed as the model resolution increases. This is caused by a drastic increase in operation counts at high resolution in the spectral scheme, which is entirely attributed to a Legendre polynomial, with a computational cost proportional to the cube of the truncated wavenumber. Most of computation

costs for semi-Lagrangian scheme consist of interpolation procedures with a PPM and monotone filter, and its operation counts are approximately proportional to the square of the model resolution, which is lower than the spectral scheme. Therefore, the computational efficiency improves as the model resolution increases. When two additional tracers are included (WSM5 + 1), the semi-Lagrangian advection

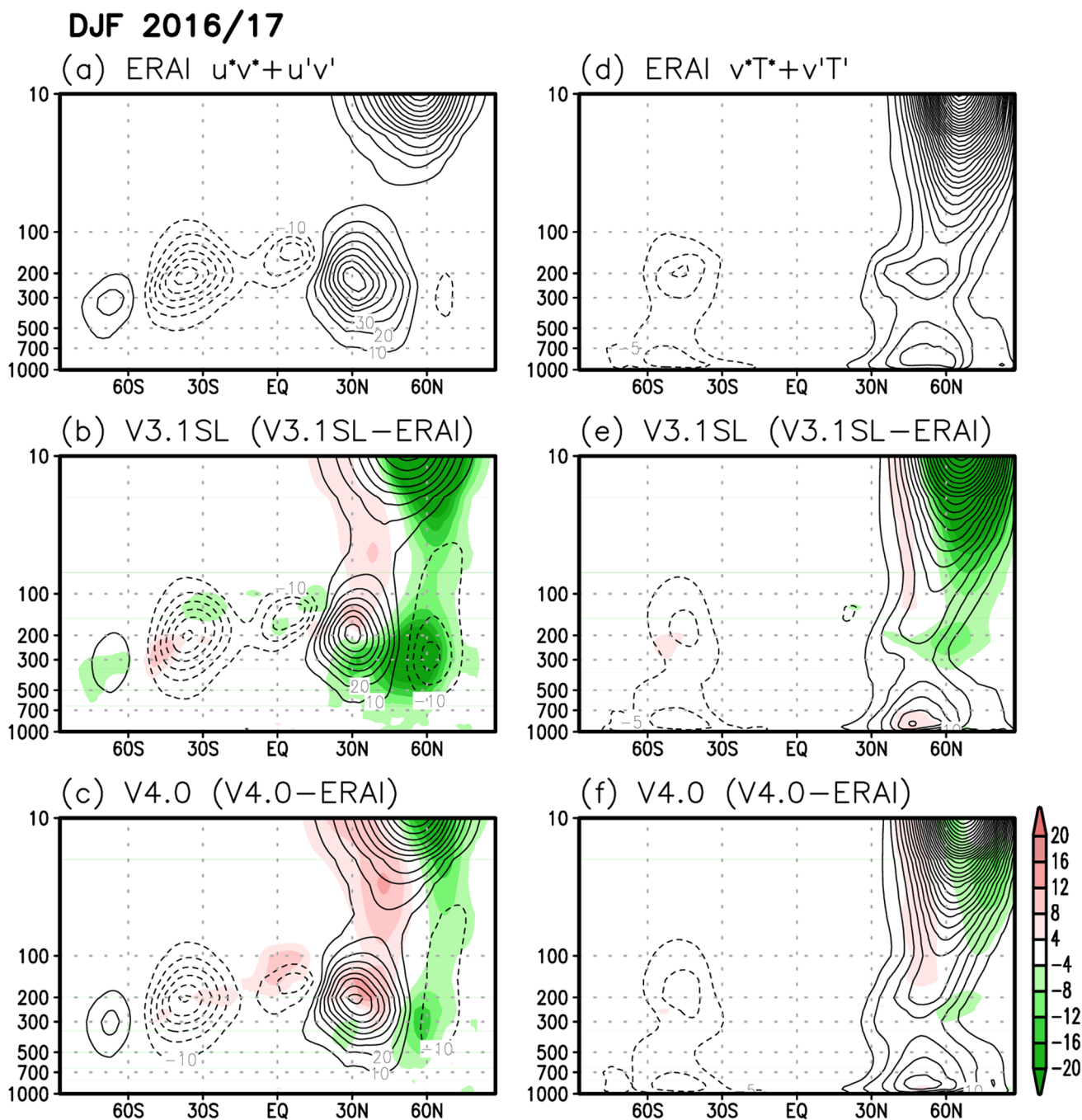


Fig. 8 Same as Fig. 7, but for DJF 2016–2017

remains more expensive than the spectral advection at low resolutions. However, the efficiency increases as the number of advected tracers increases (cf. the solid line versus the dotted line in Fig. 11). At T510 resolution, the semi-Lagrangian scheme is more efficient by approximately 35% than when the number of tracers is four. This result indicates that a computational efficiency gain is expected with an increase in the number of hydrometeors (or chemical constituents) as well as the model resolution.

6 Concluding Remarks

GRIMs-GMP version 4.0 (V4.0) is constructed with upgrades in both dynamics and physics. The original spectral advection in version 3.1 (V3.1) is replaced with a semi-Lagrangian scheme. Most physical parameterizations are advanced by transplanting the physics schemes of WRF version 4.0. The ancillary input data are also updated using the latest dataset. Aerosol and ozone concentrations are

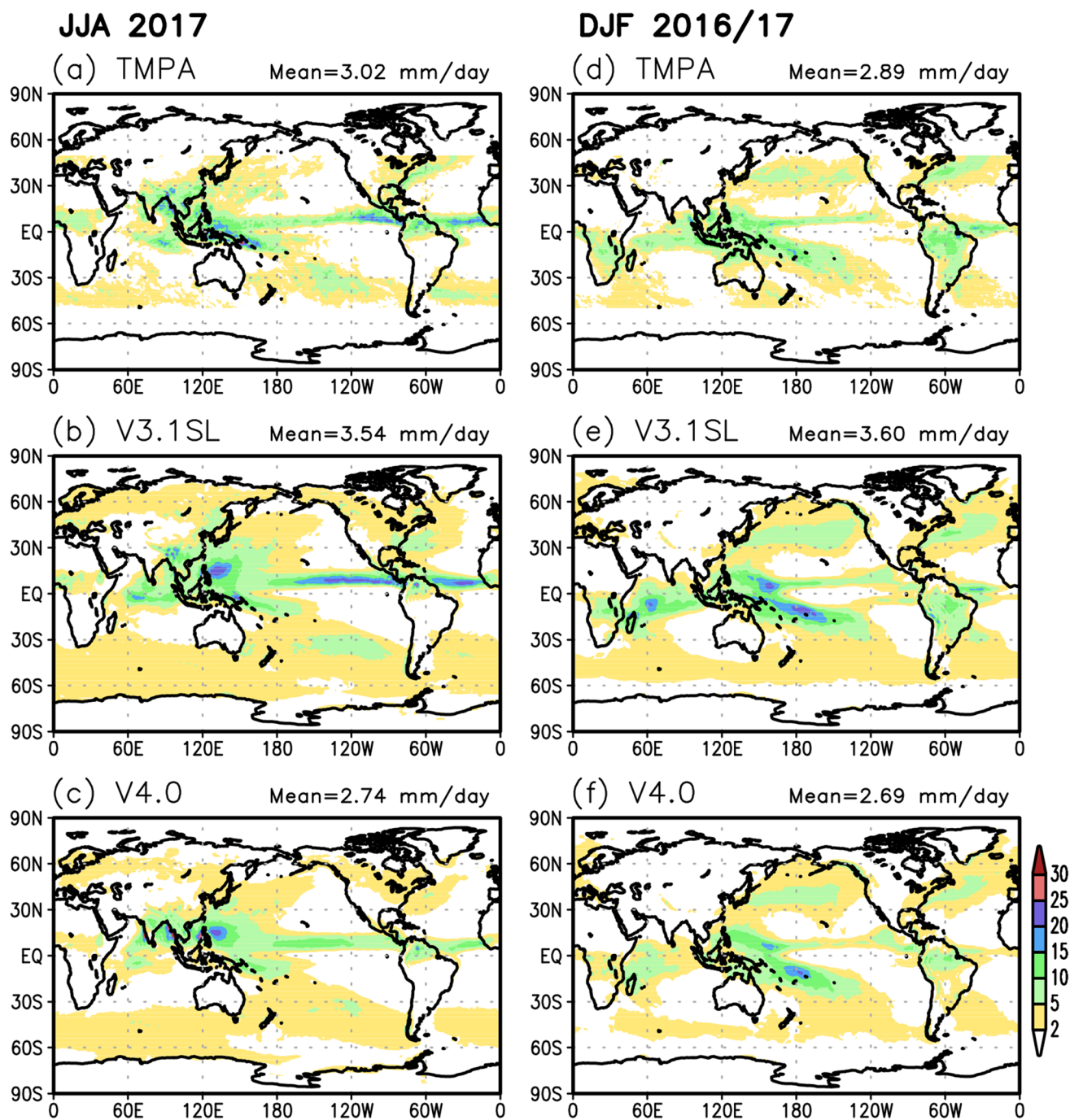


Fig. 9 Global precipitation (mm day⁻¹) averaged for (left) JJA 2017 and (right) DJF 2016–2017, obtained from a,d TMPA and simulated by b,e V3.1SL and c,f V4.0. The TMPA data covers from 50°S to 50°N

prescribed using the latest monthly climatology, whereas carbon dioxide concentrations are fixed at a constant value of 400 ppmv with no seasonal or spatial variations.

The semi-Lagrangian scheme successfully simulates the idealized test cases that effectively suppress wave-like patterns (no negative values). The field of interest is slightly smoothed due to the interpolation process with monotonicity

which could be improved with a high-order accurate monotone filter (Blossey and Durran 2008) or remapping algorithm (Zerroukat et al. 2010). In the seasonal ensemble simulations, only a slight difference is found between the spectral and semi-Lagrangian runs using WSM1 microphysics (considering specific humidity only), which indicates the successful implementation of semi-Lagrangian moisture

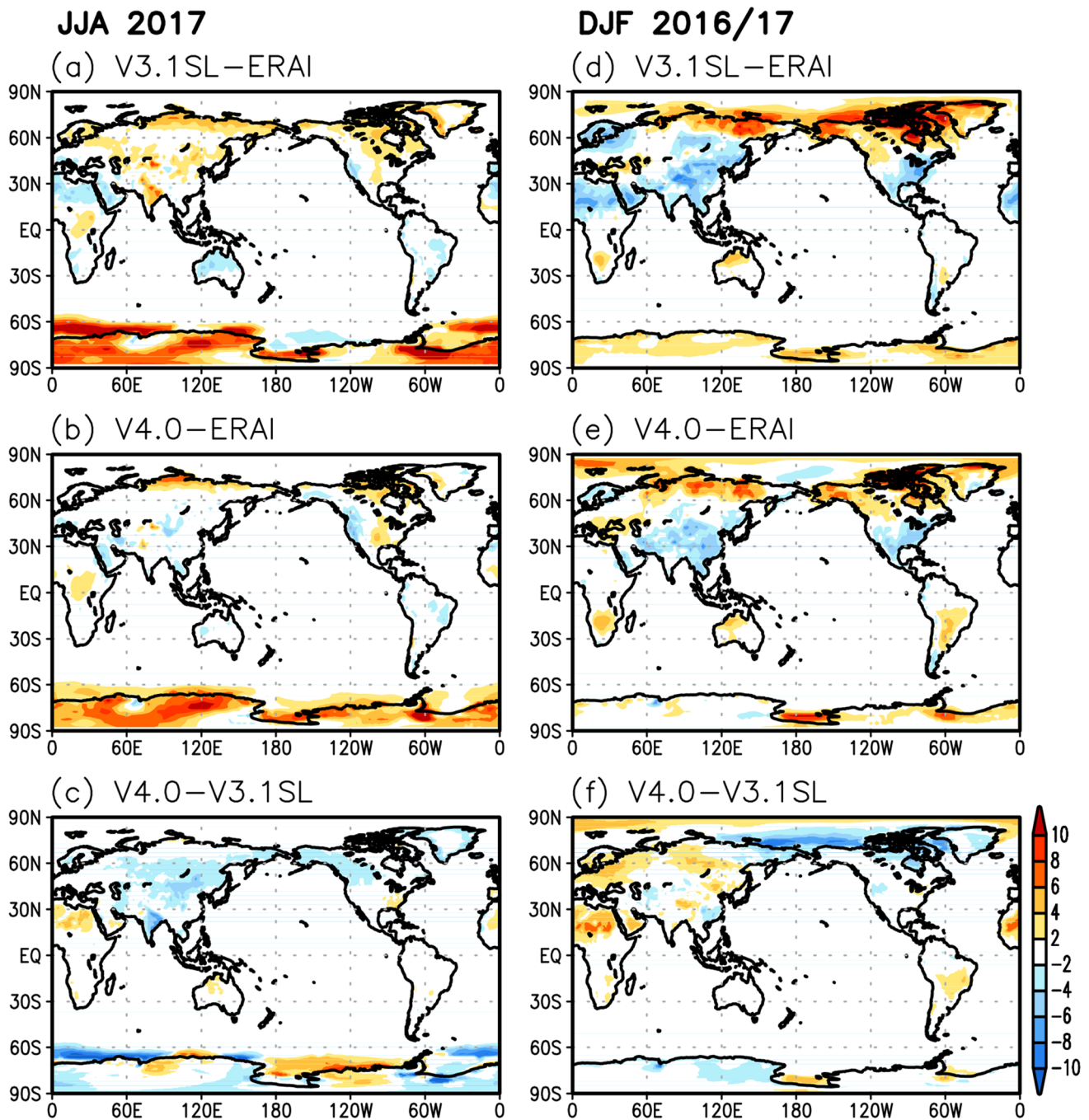


Fig. 10 Difference in 2 m air temperature (K) averaged for (left) JJA 2017 and (right) DJF 2016–2017: **a, d** V3.1SL minus ERAI, **b, e** V4.0 minus ERAI, and **c, f** V4.0 minus V3.1SL.

advection into the spectral dynamical core without significant side effects.

The new physics package and ancillary dataset in V4.0 lead to significant improvements in seasonal ensemble simulations for both dynamical and physical quantities. In the stratosphere, temperature biases are considerably reduced. The biases in the zonal-mean circulation and eddy fluxes are also significantly reduced globally. The distribution of global

precipitation becomes closer to the observation, whereas it is slightly underestimated in the new version. The near-surface temperature biases decrease across the regions during summer and winter.

As an added feature, GRIMs V4.0 support NetCDF I/O in addition to the GRIB file format. Moreover, monthly/yearly averaging is a built-in feature (i.e., on-the-fly calculation during model integration) in the new version,

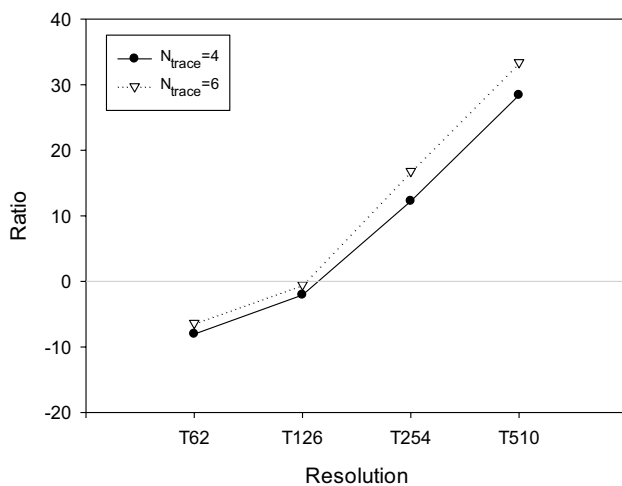


Fig. 11 Computational efficiency of semi-Lagrangian advection to spectral advection at resolutions of T62, T126, T254, and T510 with 64 vertical layers when the number of tracers is (circle) 4 and (inverted triangle) 6

thereby enabling the post-processing to be skipped for averaging the output data. Process-based time profiling is also available by utilizing the general-purpose timing library.

The overall improvements of the old version were confirmed by conducting seasonal ensemble simulations. To understand the specific effects of updated physics and ancillary data on model performance, further comprehensive analysis with additional process-wise benchmarking is required. For example, it is presumed that the updated low-level drag scheme could improve the polar stratospheric wind and temperature (Koo et al. 2018) and new ozone data could partly modulate the stratospheric temperature bias (Fig. S3). The effective hydrometeor radius is fixed in V4.0, but should be variable as it plays an important role in radiative feedback (Bae and Park 2019). The WSM5 microphysics scheme can provide improved skill scores for the precipitation amount and distribution (Fig. S4). However, this incurs a higher computational cost. Their effects on short-range forecasts must be investigated at very high resolutions (below 25 km). We will address these issues in future research.

A follow-up study will test the V4.0 performance in the Atmospheric Model Intercomparison Project (AMIP)-type simulation under the Coupled Model Intercomparison Project Phase 6 (CMIP6) standard protocol, in which the spatiotemporal variations of incoming solar constant, carbon dioxide concentrations, ozone concentrations, and others will be considered. As future plans, coupling with the chemistry model suggested by Jeong et al. (2019) and Lee et al. (2022) and the ocean/sea-ice model for climate simulation are placed on the development roadmap.

Supplementary Information The online version contains supplementary material available at <https://doi.org/10.1007/s13143-022-00297-y>.

Acknowledgements This work was supported by Korea Environment Industry & Technology Institute (KEITI) through “Climate Change R&D Project for New Climate Regime”, funded by Korea Ministry of Environment (MOE) (2022003560004). Dr. Ji-Young Han and Ji-Young Oh implemented the KSAS scheme and provided CAMS-based climatological ozone data, respectively.

Declarations

Competing Interest The authors declare no competing financial interests or personal relationship that influence the work reported in this paper.

References

- Adler, R.F., et al.: The Global Precipitation Climatology Project (GPCP) monthly analysis (New Version 2.3) and a review of 2017 global precipitation. *Atmosphere* **9**, 138 (2018)
- Bae, S.Y., Park, R.S.: Consistency between the cloud and radiation processes in a numerical forecasting model. *Meteorol. Atmos. Phys.* **131**, 1429–1436 (2019)
- Barlage, M., Zeng, X., Wei, H., Mitchell, K.E.: A global 0.05° maximum albedo dataset of snow-covered land based on MODIS observations. *Geophys. Res. Lett.* **32**, L17405 (2005)
- Blossey, P.N., Durran, D.R.: Selective monotonicity preservation in scalar advection. *J. Comput. Phys.* **227**, 5160–5183 (2008)
- Briegleb, B.P., Minnis, P., Ramanathan, V., Harrison, E.: Comparison of regional clear-sky albedos inferred from satellite observations and model computations. *J. Climate Appl. Meteorol.* **25**, 214–226 (1986)
- Butchart, N., et al.: Overview of experiment design and comparison of models participating in phase 1 of the SPARC Quasi-Biennial Oscillation initiative (QBOi). *Geosci. Model. Dev.* **11**, 1009–1032 (2018)
- Byun, Y.-H., Hong, S.-Y.: Improvements in the Subgrid-scale representation of moist convection in a cumulus parameterization scheme: the single-column test and its impact on seasonal prediction. *Mon. Wea. Rev.* **135**, 2135–2154 (2007)
- Chang, E.C., Yoshimura, K.: A semi-Lagrangian advection scheme for radioactive tracers in the NCEP Regional Spectral Model (RSM). *Geosci. Model. Dev.* **8**, 3247–3255 (2015)
- Charnock, H.: Wind stress on a water surface. *Q. J. R. Meteorol. Soc.* **81**, 639–640 (1955)
- Choi, H.-J., Hong, S.-Y.: An updated subgrid orographic parameterization for global atmospheric forecast models. *J. Geophys. Research: Atmos.* **120**, 12445–12457 (2015)
- Chou, M.-D., Suarez, M.J.: A solar radiation parameterization for atmospheric studies. NASA/TM-1999-104606, 38 pp (1999)
- Chou, M.-D., Lee, K.-T.: A parameterization of the effective layer emission for infrared radiation calculations. *J. Atmos. Sci.* **62**, 531–541 (2005)
- Chou, M.-D., Lee, K.-T., Tsay, S.-C., Fu, Q.: Parameterization for cloud longwave scattering for use in atmospheric models. *J. Clim.* **12**, 159–169 (1999)
- Chun, H.-Y., Baik, J.-J.: Momentum flux by thermally induced internal gravity waves and its approximation for large-scale models. *J. Atmos. Sci.* **55**, 3299–3310 (1998)
- Colella, P., Woodward, P.R.: The Piecewise Parabolic Method (PPM) for gas-dynamical simulations. *J. Comput. Phys.* **54**, 174–201 (1984)

- Colella, P., Sekora, M.D.: A limiter for PPM that preserves accuracy at smooth extrema. *J. Comput. Phys.* **227**, 7069–7076 (2008)
- Edmon, H.J., Hoskins, B.J., McIntyre, M.E.: Eliassen-palm cross sections for the troposphere. *J. Atmos. Sci.* **37**, 2600–2616 (1980)
- Ek, M.B., Mitchell, K.E., Lin, Y., Rogers, E., Grunmann, P., Koren, V., Gayno, G., Tarpley, J.D.: Implementation of Noah land surface model advances in the National Centers for Environmental Prediction operational mesoscale Eta model. *J. Phys. Res.* **108**, 8851 (2003)
- Gutman, G., Ignatov, A.: The derivation of the green vegetation fraction from NOAA/AVHRR data for use in numerical weather prediction models. *Int. J. Remote Sens.* **19**, 1533–1543 (1998)
- Han, J.-Y., Hong, S.-Y., Kwon, Y.C.: The performance of a revised Simplified Arakawa–Schubert (SAS) convection scheme in the medium-range forecasts of the Korean Integrated Model (KIM). *Weather Forecast.* **35**, 1113–1128 (2020)
- Han, J.-Y., Hong, S.-Y., Lim, K.-S.S., Han, J.: Sensitivity of a cumulus parameterization scheme to precipitation production representation and its impact on a heavy rain event over Korea. *Mon. Weather Rev.* **144**, 2125–2135 (2016)
- Hong, S.-Y.: A new stable boundary-layer mixing scheme and its impact on the simulated East Asian summer monsoon. *Q. J. R. Meteorol. Soc.* **136**, 1481–1496 (2010)
- Hong, S.-Y., Jang, J.: Impacts of shallow convection processes on a simulated boreal summer climatology in a global atmospheric model. *Asia-Pacific J. Atmos. Sci.* **54**, 361–370 (2018)
- Hong, S.-Y., Juang, H.-M.H., Zhao, Q.: Implementation of prognostic cloud scheme for a regional spectral model. *Mon. Weather Rev.* **126**, 2621–2639 (1998)
- Hong, S.-Y., Dudhia, J., Chen, S.-H.: A revised approach to ice microphysical processes for the bulk parameterization of clouds and precipitation. *Mon. Weather Rev.* **132**, 103–120 (2004)
- Hong, S.-Y., Noh, Y., Dudhia, J.: A new vertical diffusion package with an explicit treatment of entrainment processes. *Mon. Weather Rev.* **134**, 2318–2341 (2006)
- Hong, S.-Y., Choi, J., Chang, E.-C., Park, H., Kim, Y.-J.: Lower-tropospheric enhancement of gravity wave drag in a global spectral atmospheric forecast model. *Weather Forecast.* **23**, 523–531 (2008)
- Hong, S.-Y., et al.: The Korean Integrated Model (KIM) system for global weather forecasting. *Asia-Pacific J. Atmos. Sci.* **54**, 267–292 (2018)
- Hong, S.-Y., et al.: The Global/Regional Integrated Model system (GRIMs). *Asia-Pacific J. Atmos. Sci.* **49**, 219–243 (2013)
- Iacono, M.J., Delamere, J.S., Mlawer, E.J., Shephard, M.W., Clough, S.A., Collins, W.D.: Radiative forcing by long-lived greenhouse gases: Calculations with the AER radiative transfer models. *J. Geophys. Res.: Atmos.* **113**, D13103 (2008)
- Jeon, J.-H., Hong, S.-Y., Chun, H.-Y., Song, I.-S.: Test of a convectively forced gravity wave drag parameterization in a general circulation model. *Asia-Pacific J. Atmos. Sci.* **46**, 1–10 (2010)
- Jeong, Y.-C., Yeh, S.-W., Lee, S., Park, R.J.: A global/regional integrated model system-chemistry climate model: 1. Simulation characteristics. *Earth Space Sci.* **6**, 2016–2030 (2019)
- Juang, H.-M.H.: Semi-Lagrangian advection without iteration. In: *Proceedings of the Conference on Weather Analysis and Forecasting*, Longtan, Taoyan, Taiwan, Central Weather Bureau, 227 (2007)
- Juang, H.-M.H., Hong, S.-Y.: Forward semi-lagrangian advection with mass conservation and positive definiteness for falling hydrometeors. *Mon. Weather Rev.* **138**, 1778–1791 (2010)
- Kent, J., Ullrich, P.A., Jablonowski, C.: Dynamical core model intercomparison project: Tracer transport test cases. *Q. J. R. Meteorol. Soc.* **140**, 1279–1293 (2014)
- Kim, E.-J., Hong, S.-Y.: Impact of air-sea interaction on East Asian summer monsoon climate in WRF. *J. Phys. Res.* **115**, D19118 (2010)
- Kim, Y.-J., Arakawa, A.: Improvement of orographic gravity wave parameterization using a mesoscale gravity wave model. *J. Atmos. Sci.* **52**, 1875–1902 (1995)
- Koo, M.-S., Hong, S.-Y.: Double fourier series dynamical core with hybrid sigma-pressure vertical coordinate. *Tellus A: Dyn.* **65**, 19851 (2013)
- Koo, M.-S., Choi, H.-J., Han, J.-Y.: A parameterization of turbulent-scale and mesoscale orographic drag in a global atmospheric model. *J. Geophys. Res.: Atmos.* **123**, 8400–8417 (2018)
- Lauritzen, P.H., Jablonowski, C., Taylor, M.A., Nair, R.D.: Rotated versions of the jablonowski steady-state and baroclinic wave test cases: a dynamical core intercomparison. *J. Adv. Model. Earth Syst.* **2**, 15 (2010)
- Lee, S., Park, R.J., Hong, S.-Y., et al.: A New Chemistry-climate model GRIMs-CCM: model evaluation of interactive chemistry-meteorology simulations. *Asia-Pac J. Atmos. Sci.* (2022). <https://doi.org/10.1007/s13143-022-00281-6>
- Long, P.J.: An general unified similarity theory for the calculation of turbulent fluxes in the numerical weather prediction models for unstable condition. Office Note 302, p. 330. U.S. Department of Commerce, National oceanic and Atmospheric Administration, National Weather Service, National Meteorological Center (1984)
- Long, P.J.: An economical and compatible scheme for parameterizing the stable surface layer in the medium-range forecast model, Office Note 321, p. 324. U.S. Department of Commerce, National oceanic and Atmospheric Administration, National Weather Service, National Meteorological Center (1986)
- Lu, B., Zhong, J., Wang, W., Tang, S., Zheng, Z.: Influence of near real-time green vegetation fraction data on numerical weather prediction by WRF over North China. *J. Meteorol. Res.* **35**, 505–520 (2021)
- Mitchell, K., et al.: The community noah Land-Surface Model (LSM): User's Guide Public Release Version 2.7.1. *NCEP* (2005)
- Mocko, D.M., Cotton, W.R.: Evaluation of fractional cloudiness parameterizations for use in a mesoscale model. *J. Atmos. Sci.* **52**, 2884–2901 (1995)
- Orszag, S.A.: Transform method for the calculation of vector-coupled sums: application to the spectral form of the vorticity equation. *J. Atmos. Sci.* **27**, 890–895 (1970)
- Park, H., Hong, S.-Y.: An Evaluation of a mass-flux cumulus parameterization scheme in the KMA global forecast system. *J. Meteor. Soc. Jpn.* **85**, 151–169 (2007)
- Park, R.-S., Chae, J.-H., Hong, S.-Y.: A revised prognostic cloud fraction scheme in a global forecasting system. *Mon. Weather Rev.* **144**, 1219–1229 (2016)
- Schär, C., Leuenberger, D., Fuhrer, O., Lüthi, D., Girard, C.: A new terrain-following vertical coordinate formulation for atmospheric prediction models. *Mon. Weather Rev.* **130**, 2459–2480 (2002)
- Staniforth, A., Côté, J.: Semi-lagrangian integration schemes for atmospheric models—A review. *Mon. Weather Rev.* **119**, 2206–2223 (1991)
- Sundqvist, H., Berge, E., Kristjánsson, J.E.: Condensation and cloud parameterization studies with a mesoscale numerical weather prediction model. *Mon. Weather Rev.* **117**, 1641–1657 (1989)
- Taylor, J.P., Edwards, J.M., Glew, M.D., Hignett, P., Slingo, A.: Studies with a flexible new radiation code. II: Comparisons with aircraft short-wave observations. *Q. J. R. Meteorol. Soc.* **122**, 839–861 (1996)
- Ullrich, P.A., Jablonowski, C., Kent, J., Lauritzen, P.H., Nair, R.D., Taylor, M.A.: Dynamical Core Model Intercomparison Project (DCMIP) test case document. NCAR Tech. Doc., pp 83 (2012). Available online at http://websites.umich.edu/~cjablono/DCMIP-2012_TestCaseDocument_v1.7.pdf
- Williamson, D.L.: Semi-Lagrangian moisture transport in the NMC spectral model. *Tellus A* **42**, 413–428 (1990)

- Williamson, D.L.: The evolution of dynamical cores for global atmospheric models. *J. Meteor. Soc. Jpn.* **85B**, 241–269 (2007)
- Xu, K.-M., Randall, D.A.: A semiempirical cloudiness parameterization for use in climate models. *J. Atmos. Sci.* **53**, 3084–3102 (1996)
- Zeng, X., Wang, Z., Wang, A.: Surface skin temperature and the interplay between sensible and ground heat fluxes over arid regions. *J. Hydrometeor* **13**, 1359–1370 (2012)
- Zerroukat, M., Staniforth, A., Wood, N.: The monotonic Quartic Spline Method (QSM) for conservative transport problems. *J. Comput. Phys.* **229**, 1150–1166 (2010)
- Zhang, Y., Juang, H.-M.H.: A mass-conserving non-iteration-dimensional-split semi-Lagrangian advection scheme for limited-area modelling. *Q. J. R. Meteorol. Soc.* **138**, 2118–2125 (2012)

Publisher's Note Springer Nature remains neutral with regard to jurisdictional claims in published maps and institutional affiliations.

Springer Nature or its licensor holds exclusive rights to this article under a publishing agreement with the author(s) or other rightsholder(s); author self-archiving of the accepted manuscript version of this article is solely governed by the terms of such publishing agreement and applicable law.